Soil Dynamics and Earthquake Engineering 123 (2019) 217–229

Contents lists available at ScienceDirect

Soil Dynamics and Earthquake Engineering

journal homepage: www.elsevier.com/locate/soildyn

Uncertainty quantification and propagation in the modeling of liquefiable sands

Vicente Mercado[a], Felipe Ochoa-Cornejo[b], Rodrigo Astroza[c,*], Waleed El-Sekelly[d,e], Tarek Abdoun[e,f], Cesar Pastén[b], Francisco Hernández[b]

[a] Department of Civil and Environmental Engineering, Universidad del Norte, Barranquilla, Colombia
[b] Department of Civil Engineering, Universidad de Chile, Santiago, Chile
[c] Faculty of Engineering and Applied Sciences, Universidad de los Andes, Santiago, Chile
[d] Department of Structural Engineering, Mansoura University, Mansoura, Egypt
[e] New York University Abu Dhabi, Abu Dhabi, United Arab Emirates
[f] Department of Civil and Environmental Engineering, Rensselaer Polytechnic Institute, NY, USA

A B S T R A C T

This paper combines data from laboratory, centrifuge testing, and numerical tools to highlight the predictive capabilities of the Bayesian method for uncertainty quantification and propagation. The Bayesian approach is employed to estimate uncertain parameters of a multi-yield constitutive model using data from cyclic-triaxial testing. Then, predictive capabilities of a finite element model in reproducing the dynamic response of a saturated sand deposit are investigated by drawing samples from the estimated posterior probability distributions of the constitutive model parameters. Variability of the predicted responses due to estimation uncertainty is evaluated. The response of centrifuge tests is used to assess the simulated responses.

1. Introduction

The understanding of earthquake-induced liquefaction phenomena is of vital importance in earthquake engineering and hazard assessment. The rapid cyclic shearing of saturated loose sand induces an undrained response of granular material, increasing the excess pore water pressures with each cycle of loading and simultaneously reducing the effective stresses, and therefore, the stiffness of the soil. When excess pore pressure increases up to a value that eventually reaches the initial effective stress, a transient state of zero effective stress is reached, triggering the liquefaction of the soil, and causing significant deformations with catastrophic consequences [1,2]. The 1964 M_w 7.6 Niigata and 1964 M_w 9.2 Alaska Earthquakes highlighted the crucial and devastating effects of liquefaction on modern geotechnical and civil infrastructure [3]. Recently, large earthquakes, such as the 2010 M_w 8.8 Maule [4], 2010 M_w 7.1 Christchurch [5], and the 2011 M_w 9.0 Tohoku Earthquakes [6] have also presented severe cases of liquefaction in sandy soil deposits. In addition, and provided the described context above, other liquefaction criteria have been defined, with the intention to consider the large deformations -that occur at a high rate- once the 100% of excess pore pressures are reached in triaxial testing. These criteria consider 2.5, 5, and 10% of axial deformations in double amplitude [7,8]. These definitions are very useful for liquefaction design, although liquefaction characterization is difficult at large strains, generally due to equipment compliance as the strain rates are significantly high.

Liquefaction has been widely studied in the laboratory as well as in the field. On the one hand, laboratory studies have considered the use of apparatuses that can apply cyclic shear loading and an undrained response in either stress or strain controlled conditions, causing liquefaction. Among the most common equipment are cyclic triaxial, direct simple shear, and torsional shear tests, which are used to investigate the dynamic behavior and pore pressure response of soils subjected to cyclic loading [9]. These tests, however, are affected by sampling disturbance and are limited in their ability to replicate stress paths observed in the field [9]. On the other hand, in the field, standard engineering practices in the assessment of liquefaction are usually based on tests such as the Standard Penetration Test (SPT), Cone Penetration Test (CPT), or in-situ shear wave velocity tests [10–12]. These methodologies have been empirically calibrated based on field case histories of liquefaction and no liquefaction cases, leading to quite reliable results. Other alternative approaches present significant opportunities to be considered for liquefaction studies, including strain-based and energy-based approaches, as well as computational approaches [11,13].

In the context described above, physical modeling appears as a significant and appealing alternative to overcome laboratory and field testing drawbacks to study liquefaction phenomena. In the last decades, advances in physical modeling, including large-scale [14–16] and

* Corresponding author.
E-mail address: rastroza@miuandes.cl (R. Astroza).

https://doi.org/10.1016/j.soildyn.2019.04.016
Received 20 February 2019; Accepted 11 April 2019

centrifuge testing [17,18], have led to improved capabilities in representing the in-situ conditions of saturated soils under earthquake loading and liquefaction phenomena. Centrifuge modeling is particularly advantageous since scaling allows reduced-scale models to represent the full scale of the field conditions at a fraction of the cost of a large-scale test [19]. Although it has been recognized that there is significant variability in centrifuge modeling of excited soil deposits, recent research efforts have shown improved capabilities in the consistency and repeatability of the centrifuge modeled response [17,20]. Dobry et al. [21], for instance, confirmed that centrifuge testing could reproduce realistic results in agreement with the liquefaction response of sandy deposits in the field subjected to the 1989 M_w 6.9 Loma Prieta Earthquake in California.

In spite of the significant contribution that laboratory, field testing, and physical models have provided to the state of the art on liquefaction phenomena, the development of numerical simulations with well-defined theoretical constitutive models is often the only viable tool for the estimation of the dynamic and pore pressure response of specific sites prone to liquefaction. Such analyses require a precise geotechnical characterization and the selection of a suitable constitutive model. Some plasticity-based constitutive models have been developed to predict the stress-strain and pore water pressure response of granular soils [22–25]. Mechanics-based numerical methods incorporating such constitutive models are being employed increasingly in engineering practice due to their cost efficiency and their detailed prediction capabilities for the evaluation of the liquefaction potential of soil deposits [13,26,27]. Remarkable efforts such as VELACS [28] and LEAP [17,27,29], have been devoted to better understand the variability associated to numerical modeling. Prevost and Popescu [28], for instance, reported "Class A" numerical predictions yielding a close estimation of the recorded pore pressure response of several experimental models. However, several authors have highlighted the need for further efforts in the assessment of the capabilities and accuracy of the available computational tools [29,30].

Since any numerical model is an approximation of the system being represented, when using a numerical tool to predict the response of a dynamic system, different sources of uncertainty arise because of the random nature of the problem being tackled. These sources of uncertainty are usually categorized into model parameter uncertainty, model structure uncertainty (i.e., modeling errors), and measurement noise. In particular, an adequate numerical prediction of the dynamic and pore pressure response of a seismically excited soil deposit requires a suitable calibration of the model parameters. Different model updating approaches, including those of deterministic and probabilistic nature, have been proposed and investigated in laboratory settings and site characterization problems [31–39]. In this context, the effect of different sources of uncertainty, including material spatial variability, modeling uncertainty, and measurement noise, are significant [40,41] and lead to significant levels of uncertainty in the identification of model parameters [32,42,43]. The effect of the uncertainty in model parameters on the estimation of a deposit's dynamic response is often unknown or ignored; the reliability and variability of predicted acceleration and pore pressure time histories associated to model parameter uncertainty are usually not well understood [41]. Some authors have studied the effects of spatial variability on the response of geotechnical systems [44–47], and yet there is still a need to better assess the impact of the uncertainty in the calibration of the parameters on the modeled dynamic response of liquefiable sandy soil deposits.

This study presents the implementation of a Bayesian (probabilistic) approach accounting for distinct sources of uncertainty for the calibration of constitutive soil models in order to achieve a better understanding of the predictive capabilities of numerical simulations in the response of liquefiable soils. For the presented analysis, experimental data from undrained cyclic triaxial testing conducted on clean Ottawa sand [8] is first employed to estimate the model parameters of a pressure-dependent multi-yield constitutive model (PDMY02) [22,48]. A Bayesian estimation approach is used, obtaining the joint probability density function (PDF) of the model parameters to be estimated. These analysis results are then used to assess the effects of the uncertainty in the identified parameters on the predictive capabilities of a finite element (FE) model in simulating the dynamic response of a saturated sand deposit. Samples from the posterior PDF of the model parameter estimated using the triaxial test data are drawn; then the estimation uncertainties are propagated through the FE model to compare measured and FE-predicted responses (acceleration and pore water pressure time histories). Numerical predictions are compared to the response of reduced-scale centrifuge models tested in a laminar box using the geotechnical centrifuge at the Rensselaer Polytechnic Institute (RPI). It is worth noting that the analysis of large shear deformations generated at low confinement is excluded in this work because of the considerable variability observed in both laboratory settings and numerical simulations. Centrifuge tests, for instance, have shown significant variability in the achieved permanent displacement of excited deposits [30]. In addition, since the characterization of large strain response is often compromised in conventional laboratory settings due to equipment compliance at such high strain rates, the validation of the permanent displacement response of numerical models still poses an unsolved challenge [30]. The consideration of these large displacements into the presented analysis would require considerable increased complexity into the implemented material characterization, which is beyond the scope of this paper.

The objective of this work is to illustrate the capabilities of the Bayesian technique to estimate the parameters of a constitutive soil model using laboratory test data, and to quantify the uncertainty associated to the calibration procedure, while assessing correlations between estimated parameters. It also intends to show that an adequate characterization of the uncertainty in the estimated parameters of the constitutive model allows for a proper assessment of the modeled dynamic response of a deposit subjected to base acceleration. It is worth noting that the procedure presented in this paper is of significant relevance for current engineering applications; in engineering practice, the response of a soil deposit is typically predicted based on scarce laboratory data conducted to characterize the soil properties. An adequate quantification of the uncertainty in the modeled response associated to the calibration process will result in improved credibility and better understanding of the predictive capabilities of available computational tools.

2. Soil triaxial testing

2.1. Soil material description

The soil used is clean uniform silica Ottawa Sand (C_u = 1.9, C_c = 0.89), with particle size distribution in the fine-to-medium range (0.10–0.60 mm), with less than 1% of fines. Sand particles have rounded to subrounded shape, soft gray color, and diameters ranging between 0.15 mm and 0.85 mm (D_{10} ~ 0.2 mm, D_{30} ~ 0.26 mm, D_{50} ~ 0.33 mm, D_{60} ~ 0.38 mm, Fig. 1a). The maximum and minimum void ratios are e_{min} = 0.480 and e_{max} = 0.783 [8]. Fig. 1b shows Scanning Electron Microscope (SEM) images of clean Ottawa sand grains, obtained using an FEI Quanta 3D field emission SEM. Imaging of the sand was conducted in low vacuum mode using a low vacuum secondary electron detector (LVSED). The images illustrate the uniform size and rounded nature of Ottawa sand and highlight a rather “smooth” surface topography of the grains. In the context of the chart proposed by Krumbein and Sloss [49], particles present a sphericity between 0.7 and 0.9 and a roundness between 0.5 and 0.7.

2.2. Experimental setup

The experimental data were obtained from cyclic undrained consolidated triaxial testing performed on the Ottawa sand described in

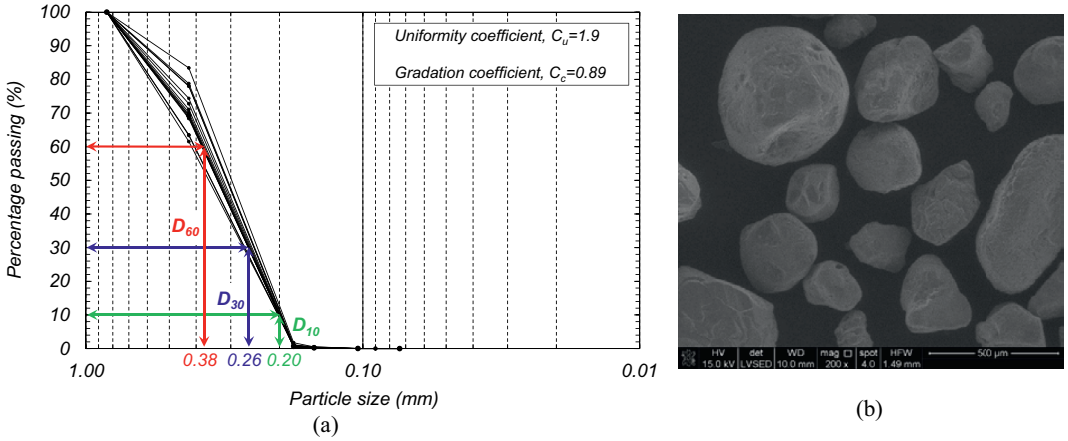

Fig. 1. (a) Ottawa sand grain size distribution, and (b) SEM image of a group of Ottawa sand particles [7].

Section 2.1. The setup used to obtain this type of data was the CKC system (Soil Testing Equipment) [7,8]. The sand specimen for cyclic testing was prepared by dry pluviation, an efficient technique to build laboratory sand specimens, preventing particle crushing, and reducing segregation [50,51]. The sand was placed in a sealed plastic container which is connected to a copper pipe of 15 cm length to control the pluviation and a valve to control the sand flow. The material was pluviated inside the triaxial split mold (covered with latex membrane) to build the cylindrical specimens with geometrical dimensions of 15 cm in length and 7 cm in diameter. The initial dry density of the soil was of 1590 kg/m^3, with a skeleton relative density $D_r = (e_{max} - e)/(e_{max} - e_{min}) \approx 40\%$ based on the skeleton void ratio e and the limiting void ratios e_{max} and e_{min}. The sand specimens were flushed with carbon dioxide (CO_2) to reduce the maximum amount of air in the void volume of the sand specimen, to ease the permeation of deaired deionized water in the granular sand matrix. Once the specimen reached saturation from an experimental perspective, i.e. $B_{value} > 0.95$, the sample was isotropically consolidated to an effective initial mean confining stress of $p' = 100$kPa. After consolidation, the drainage valves were closed, and the cyclic shearing was initiated. Cyclic loading under undrained conditions was performed by applying a sinusoidal deviatoric vertical stress (q) at a loading frequency of 1 Hz. During cyclic loading, the response of the soil was monitored in terms of the vertical axial strain (ε_1) and the generated excess pore pressure $\Delta u = u - u_0$, where u is the measured total pore pressure and u_0 is the initial hydrostatic pore pressure. More details on the experimental setup are given in Ochoa-Cornejo et al. [7,8]. The experiment results are discussed along with numerical modeling results in Section 4.2.

3. Soil constitutive model

There is a significant amount of studies related to the numerical modeling of soil liquefaction and flow failure of sands [52]. This study implements the PDMY02, which stands for Pressure-Dependent Multi-Surface Plasticity Model [22,48], available in the open-source software platform OpenSees [53]. This model has known limitations such as a lack of a formal expression for state dependence and the omission of Lode angle effects [22]. However, the model offers considerable simplicity in the definition of its constituting material parameters and has been successfully implemented in the prediction of the seismic response of geotechnical systems [54,55].

The multi-yield function approach introduces a set of several conical surfaces in the principal stress space, with the hydrostatic axis coincident with the apex of all the surfaces (Fig. 2a). The hardening rule to generate the hysteretic response under any arbitrary cyclic shear loading is a modified version of the Mroz Hardening Rule [56], in which the yield surfaces translate in stress space within the failure envelope. The translation of the yield surfaces enables a hysteretic and path dependent stress-strain response. The configuration of the yield surfaces allows for a piecewise linear approximation of the stress-strain behavior of the material. Relevant aspects of the model are briefly summarized below. More details on the Multi-Surface Plasticity Models can be found elsewhere [22,57].

3.1. Stress-strain

The implemented model represents the nonlinear stress-strain behavior of the soil by introducing a definition of the backbone curve proposed by Kondner [59]:

$$\tau = \frac{G_{max}\gamma}{1 + \gamma/\gamma_{ref}} \tag{1}$$

In Equation (1), τ and γ are shear stress and strain, respectively, G_{max} is the small-strain shear modulus at a reference mean effective confining pressure p'_r, $\gamma_{ref} = \tau_{max}/G_{max}$ is a reference shear strain at p'_r, and τ_{max} is the shear strength of the soil at p'_r. The shear strength at p'_r can also be expressed in terms of the shear strength friction angle of the soil, ϕ, and is given by:

$$\tau_{max} = G_{max}\gamma_{ref} = \frac{2\sqrt{2}\sin\phi}{3 - \sin\phi}p'_r \tag{2}$$

The stiffness dependency of the material with respect to the effective confining pressure p' is given by $G = G_{max}(p'/p'_r)^d$, where G is the small-strain shear modulus at a mean confining pressure p' , and d is a material parameter considered equal to 0.5 as suggested for sands [9]. In this work an arbitrary value of $p'_r = 100$ kPa ($\approx$1 atm) has been used for convenience; therefore reported values of G_{max} correspond to an effective mean confining pressure of 100 kPa. The bulk modulus of the soil skeleton, B, relates to the shear modulus by $B = 2G(1 + \nu)/(3 - 6\nu)$, where ν is the Poisson's ratio.

3.2. Flow rule

This model introduces a non-associative rule to define the plastic flow. The deviatoric component of the plastic strain increment is normal to the yield surfaces, while the rate of plastic volumetric strain is defined based on the phase transformation (PT) surface concept [60]. This surface indicates a transition in the behavior of the soil from contractive to dilative under monotonic undrained shear loading, as depicted in Fig. 2b. Following suggestions of the pioneering work of Prevost [57], the location of the stress state is inferred based on the value of the stress ratio $\eta = q/p'$, where q is the von Mises stress. If the stress ratio along the PT surface is defined as η_{PT}, then for stress states having $\eta < \eta_{PT}$ (loading inside the PT surface), or for $\eta > \eta_{PT}$ (loading

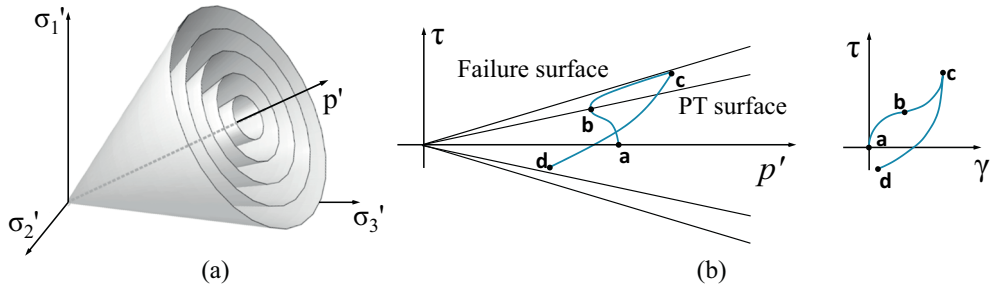

Fig. 2. (a) Graphic representation of the yield functions, and (b) schematic response for undrained shear loading [22,57,58].

outside the PT surface) with $\dot{\eta} < 0$ ($\dot{\eta}$: time rate of η), the soil will exhibit a contractive tendency under undrained loading (see stress paths from ***a*** to ***b*** and from ***c*** to ***d*** in Fig. 2b). For stress states having $\eta > \eta_{PT}$ (loading outside the PT surface) with $\dot{\eta} > 0$, the soil will exhibit a dilative tendency (see stress path from ***b*** to ***c*** in Fig. 2b). The stress ratio associated to the PT surface can also be expressed in terms of a PT angle, ϕ_{PT}, as follows:

$$\eta_{PT} = \frac{6\sin\phi_{PT}}{3-\sin\phi_{PT}} \tag{3}$$

For loading associated to a contractive tendency, the flow rule is defined by:

$$\frac{\dot{\varepsilon}_{vol}^{\,p}}{\dot{\varepsilon}_{eq}^{\,p}} = -c_1\frac{3\sqrt{6}}{2}\left[\frac{\eta}{\eta_{PT}} - 1\right]^2 \tag{4}$$

In Equation (4), $\dot{\varepsilon}_{vol}^{\,p}$ and $\dot{\varepsilon}_{eq}^{\,p}$ are the volumetric and deviatoric plastic strain increments, respectively, defined as $\dot{\varepsilon}_{vol}^{\,p} = tr(\dot{\boldsymbol{\varepsilon}}^p)$, and $\dot{\varepsilon}_{eq}^{\,p} = \sqrt{\frac{2}{3}\dot{\boldsymbol{\varepsilon}}_{dev}^{\,p}:\dot{\boldsymbol{\varepsilon}}_{dev}^{\,p}}$, where $\dot{\boldsymbol{\varepsilon}}_{dev}^{\,p} = \dot{\boldsymbol{\varepsilon}}^p - \frac{1}{3}\dot{\varepsilon}_{vol}^{\,p}\boldsymbol{\delta}$ (with $\boldsymbol{\delta}$: second-order identity tensor). The parameter $c_1 > 0$ is a material constant to add flexibility in adjusting the volumetric response. Under undrained conditions, a larger c_1 represents a larger contractive tendency in the material, resulting in a higher pore water pressure buildup rate.

For loading associated to a dilative tendency, the flow rule is defined by:

$$\frac{\dot{\varepsilon}_{vol}^{\,p}}{\dot{\varepsilon}_{eq}^{\,p}} = (1+d_1)\frac{3\sqrt{6}}{2}\left[\frac{\eta}{\eta_{PT}} - 1\right]^2 \tag{5}$$

In Equation (5), $d_1 > 0$ is a calibration constant controlling the dilative tendency of the soil.

4. Model calibration and uncertainty quantification

4.1. Parameter estimation approach

4.1.1. Bayesian inference

The technique of Bayesian inference updates the probability distributions of a set of uncertain model parameters $\Theta_m \in \mathbb{R}^{n_m\times 1}$ that define a model class $\mathscr{M}_m$ based on a set of measured responses $\mathbf{y} = \{\mathbf{y}_i \in \mathbb{R}^{n_y\times 1},\ i = 1,...,r\}$, where n_y is the number of measured responses and r denotes the number of data points in each response. The discrepancy between the observed (measured) data and the prediction of the model at a discrete time t_i can be expressed as

$$\mathbf{e}_i = \mathbf{y}_i - \mathbf{h}_i(\Theta_m|\mathscr{M}_m) \tag{6}$$

In Equation (6), $\mathbf{h}_i(\cdot)$ is the nonlinear response function of a model belonging to the class $\mathscr{M}_m$ and $\mathbf{e}_i$ is the prediction error at time t_i and includes the effects of uncertainties in the measurement, computation, and modeling. Herein, the model class for the prediction error and the variables parametrizing the prediction error are denoted by $\mathscr{M}_e$ and $\Theta_e \in \mathbb{R}^{n_e\times 1}$, respectively. Based on previous information available, prior probability distributions can be assigned to the model parameters and the prediction error parameters, denoted by $\pi_m(\Theta_m|\mathscr{M}_m)$ and $\pi_e(\Theta_e|\mathscr{M}_e)$, respectively. Then, the Bayes' theorem is used to update the combined parameter vector $\Theta = (\Theta_m, \Theta_e) \in \mathbb{R}^{(n_m+n_e)\times 1}$ given the observed (measured) data $\mathbf{y}$ and the model classes $\mathscr{M}_m$ and $\mathscr{M}_e$, i.e., to obtain the posterior probability distribution of the parameters,

$$p(\Theta|\mathbf{y},\mathscr{M}) = \frac{p(\mathbf{y}|\Theta,\mathscr{M})\cdot\pi(\Theta|\mathscr{M})}{p(\mathbf{y}|\mathscr{M})} \tag{7}$$

In Equation (7), $\pi(\Theta|\mathscr{M}) = \pi_m(\Theta_m|\mathscr{M}_m)\cdot\pi_e(\Theta_e|\mathscr{M}_e)$ is the combined prior probably distribution of the parameters, i.e., the parameters Θ_m and Θ_e are considered independent, $\mathscr{M} = \{\mathscr{M}_m, \mathscr{M}_e\}$, $p(\mathbf{y}|\Theta,\mathscr{M})$ is the likelihood function, and $p(\mathbf{y}|\mathscr{M}) = \int_{\Theta} p(\mathbf{y}|\Theta,\mathscr{M})\cdot\pi(\Theta|\mathscr{M})d\Theta$ is the evidence of the model class $\mathscr{M}$, where $\boldsymbol{\Theta}$ denotes the parameter space of Θ, and is chosen such the posterior probability distribution $p(\Theta|\mathbf{y},\mathscr{M})$ integrates to one.

4.1.2. Model class of the prediction error

A Gaussian distribution with zero mean and time-invariant covariance matrix $\boldsymbol{\Sigma}(\Theta_e) \in \mathbb{R}^{n_y\times n_y}$ is assumed for the prediction error, i.e., $\mathbf{e}_i \sim \mathcal{N}(\mathbf{0}, \boldsymbol{\Sigma}(\Theta_e))\ \forall\ \ i = 1, ...,r$ [61]. It is also assumed that the prediction errors are uncorrelated between different measurements and therefore $\boldsymbol{\Sigma}(\Theta_e)$ is a diagonal matrix with entries corresponding to the variances associated to the different measured responses, i.e., $\boldsymbol{\Sigma}(\Theta_e) = \sigma_j^2\cdot\delta_{jk}$ where δ_{jk} is the Kronecker Delta, with $j = k = 1, ...,n_y$, while σ_j are the standard deviations to be determined by the Bayesian estimation.

4.1.3. Likelihood function

Based on the assumption that the prediction error is modeled as a stationary, zero-mean, independent Gaussian noise vector process, from Equation (6) it is obtained that the likelihood function is given by [62]:

$$p(\mathbf{y}|\Theta,\mathscr{M}) = \prod_{i=1}^{r}\frac{|\boldsymbol{\Sigma}(\Theta_e)|^{-1/2}}{(2\pi)^{n_y/2}}\cdot\exp\left[-\frac{1}{2}J_i(\Theta;\mathscr{M})\right] \tag{8}$$

In equation (8), the term $J_i(\Theta;\mathscr{M})$ is given by:

$$J_i(\Theta;\mathscr{M}) = [\mathbf{y}_i - \mathbf{h}_i(\Theta_m|\mathscr{M}_m)]^T\boldsymbol{\Sigma}^{-1}(\Theta_e)[\mathbf{y}_i - \mathbf{h}_i(\Theta_m|\mathscr{M}_m)] \tag{9}$$

Equation (9) represents the weighted goodness of fit between the observed and model-predicted responses.

4.1.4. Prior probability distributions

When the amount of data is small, the prior probability distributions may significantly influence the posterior probability distributions of Θ, therefore, usually non-informative priors (uniform probably distributions) are assumed. Likewise, when the number of model parameters to be estimated is large, Gaussian prior may help to avoid identifiability problems [63].

4.1.5. Posterior probability distributions

When a significant amount of data is available, $p(\Theta|\mathbf{y},\mathscr{M})$ can be approximated by a Gaussian distribution centered at the most probable value for the model parameters and the uncertainty in the estimation

can be approximated by the inverse of the Hessian matrix evaluated at the most probable parameter values [64]. Otherwise, the solution of multi-dimensional integrals should be performed. However, these cannot be directly computed in most problems involving several parameters to be estimated, and therefore, sampling algorithms (e.g., Metropolis-Hastings, Gibss, Markov Chain Monte Carlo, and Slice) [65] are employed to approximate the posterior joint probability distribution of the model parameters using Equation (7).

From the estimated posterior probability distributions of the model parameters, an estimate of the model parameters can be computed. Usually, the *maximum a posteriori* ($\hat{\Theta}^{MAP}$) is employed, which can be obtained from the maximum of the posterior probability distribution, i.e.,

$$\hat{\Theta}^{MAP} = \arg\max_{\Theta}[p(\Theta|\mathbf{y}, \mathcal{M})] \tag{10}$$

Equivalently, from the minimum of the negative natural logarithm ($\ln[\cdot]$) of the posterior probability distribution, i.e.,

$$\hat{\Theta}^{MAP} = \arg\min_{\Theta}[-\ln[p(\mathbf{y}|\Theta, \mathcal{M})] - \ln[\pi(\Theta|\mathcal{M})]] \tag{11}$$

4.2. Model updating results

The Bayesian approach is employed to calibrate the numerical model presented in Section 3 using the experimental data collected from the laboratory cyclic triaxial test described in Section 2. Only one test was used for the model updating since the use of several tests would introduce further uncertainty associated to test-to-test variability, while this works focuses on estimation of uncertainties stemming exclusively from the model calibration procedure. Furthermore, the use of only one test is representative of common engineering practice, in which the availability of laboratory data is often limited. Other laboratory tests, however, are used for verification purposes in Section 4.3.

Stresses from the experimental triaxial test are introduced into the numerical formulation of the constitutive model described in Section 3 along with a set of parameters, Θ_m, to predict a material response, $\mathbf{h}$, defined in terms of strains and pore water pressure. The measured response vector is assembled as $\mathbf{y}_i = \left[\frac{(\varepsilon_v)_i}{(\varepsilon_v)_{\max}}, \frac{(u)_i}{(u)_{\max}}\right]^T$, where $(\varepsilon_v)_i$ and $(u)_i$ are the vertical strain and the excess pore water pressure from the triaxial test measured at time t_i, respectively, and $(\varepsilon_v)_{\max}$ and $(u)_{\max}$ are the maximum measured values of vertical strain and the excess pore water pressure, respectively. The modeled response vector is likewise assembled as $\mathbf{h}_i = \left[\frac{(\varepsilon_v^m)_i}{(\varepsilon_v^m)_{\max}}, \frac{(u^m)_i}{(u^m)_{\max}}\right]^T$, where $(\varepsilon_v^m)_i$ and $(u^m)_i$ are the vertical strain and the excess pore water pressure estimated through the constitutive model at time t_i, respectively, and $(\varepsilon_v^m)_{\max}$ and $(u^m)_{\max}$ are corresponding maximum values of vertical strain and the excess pore water pressure from the numerical modeling. The vector of model parameters to be estimated are $\Theta_m = [\phi \;\; G_{\max} \;\; \phi_{PT} \;\; \nu \;\; c_1 \;\; d_1]^T \in \mathbb{R}^{6\times 1}$, and a single standard deviation is considered as a prediction error parameter, i.e., $\Theta_e = \sigma_e \in \mathbb{R}^{1\times 1}$. Therefore, the parameter vector to be estimated is $\Theta = [\phi \;\; G_{\max} \;\; \phi_{PT} \;\; \nu \;\; c_1 \;\; d_1 \;\; \sigma_e]^T \in \mathbb{R}^{7\times 1}$. Gaussian prior probability distributions with the mean and standard deviation shown in Table 1 are assumed, with $\mathcal{N}(\mu, \sigma)$ denoting a Gaussian distribution with mean μ and standard deviation σ. Mean values were estimated based on previous analysis of laboratory results [7,66], and standard deviations were selected based on estimations suggested by previous geotechnical research [40]. Prior probability distributions for parameters specific to the implemented constitutive model (namely, c_1 and d_1) were selected based on recommended ranges by Yang et al. [48].

Table 1
Prior probability distributions assumed for the model parameters to be estimated.

Parameter	Prior	Parameter	Prior
ϕ	$\mathcal{N}(35°, 5°)$	c_1	$\mathcal{N}(0.1, 0.06)$
$G_{\max}$	$\mathcal{N}(93000\ kPa, 2500\ kPa)$	d_1	$\mathcal{N}(0.1, 0.05)$
ϕ_{PT}	$\mathcal{N}(30°, 5°)$	σ_e	$\mathcal{N}(0.2, 0.4)$
ν	$\mathcal{N}(0.3, 0.1)$		

The slice sampling algorithm [67] is used to draw 5000 samples from the natural logarithm of the posterior probability distribution. The slice sampling method is attractive because it automatically adjusts the step size to match the characteristics of the posterior PDF. To generate samples after the Markov chain has reached stationarity, 500 samples are first generated and discarded before the 5000 final samples are generated. Fig. 3 shows the samples drawn from the posterior distribution of the model parameters. Marginal distributions are depicted in the diagonal entries of the plot matrix, where the prior distributions (unnormalized) are shown in red color and the histograms of the posterior distributions in dark blue. In these plots, a total of ten bins is considered, and the frequency counts of the highest bin are shown at the top-right corner. Table 2 summarizes some statistics of the parameter estimation results, including the *maximum a posteriori* values (MAP), mean values (μ), standard deviations (σ), and coefficients of variations (*c. o. v.*). The off-diagonal panels of Fig. 3 plot the projection of the samples in the corresponding two-dimensional spaces of the model parameters. These plots show the inter-relationships between the different parameters, where the positive correlation between ϕ and ϕ_{PT} and the strong negative correlation between ν and c_1 are observed. The correlation between ϕ and ϕ_{PT} suggests that for the development of the recorded experimental increase and decrease of excess pore water pressure associated to the contractive and dilative phases of the soil, a certain ratio between ϕ and ϕ_{PT} must be maintained. It is possible that some of the scatter in the distribution of ϕ may be attributed to the fact that the constitutive model does not incorporate the Lode angle effect and thus it does not differentiate between shear strength in triaxial compression and extension. The strong negative correlation between ν and c_1 is expected given that both parameters have a direct incidence on the volumetric deformations of the material. As mentioned earlier, a larger value of c_1 results in a higher tendency towards volumetric contraction (Equation (4)), while a larger value of ν, on the other hand, yields a larger bulk modulus (B) which results in a reduced tendency towards volumetric contraction. There is also evidence of some degree of positive correlation between ϕ and c_1 and ϕ_{PT} and d_1. This is expected since, as evidenced by Equations (4) and (5), the definition of the volumetric rate of plastic strains depends on both contractive and dilative calibration parameters c_1 and d_1, as well as on the location of the PT surface, which is related to ϕ and ϕ_{PT}. Finally, some minor negative correlation between ν and d_1 is also detected. This can also be explained by the volumetric effects of both parameters. As expected, σ_e is not correlated to the material model parameters. The inter-parameter correlations imply that the prediction capabilities of the model do not change significantly if the correlated parameters are increased/decreased appropriately. It is noted that a high value is estimated for the Poisson ratio (see Table 2); this is due to its high correlation with parameter c_1. These identifiability issues can be improved if more information (from measurement data or in the prior distributions) is included in the goodness of fit between the observed and model predicted responses (see Equation (9)).

Fig. 4 shows the excess pore water pressure response and the resulting vertical strains for the experimental triaxial test. This figure also shows the numerical response obtained by using MAP of model parameters. Ranges for numerical responses computed for 100 selected samples of Θ_m are also shown in Fig. 4. These 100 samples were randomly selected from the generated Markov chain, considering only sets of parameters for which each of the model parameters were within one standard deviation of the mean values of the posterior distributions. Computed excess pore pressure responses show a good agreement with the experimental response. Amplitudes of computed vertical strains, on the other hand, are somewhat lower than the experimental ones

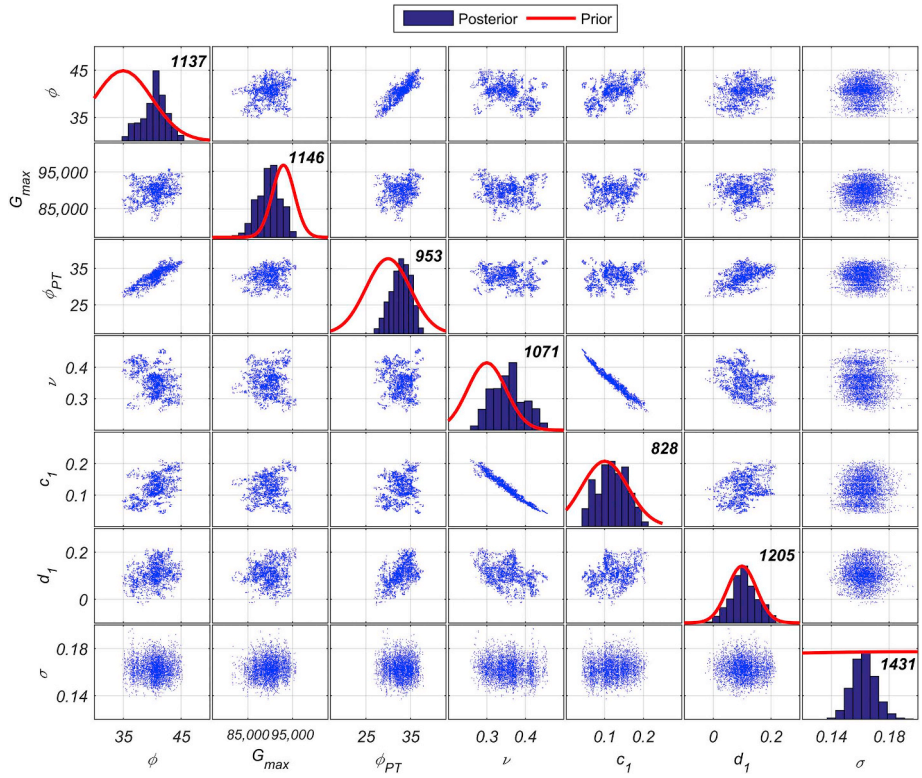

Fig. 3. Parameter estimation results for the constitutive soil model using the cyclic triaxial test data: marginal distributions in the diagonal and scatter plots of the sampled posterior distributions in the off-diagonal entries.

Table 2
Statistics of the marginal distributions of the model parameters.

Parameter	ϕ (°)	$G_{\max}$ (kPa)	ϕ_{PT} (°)	ν (−)	c_1 (−)	d_1 (−)	σ_e (−)
MAP	40.7	90820	32.9	0.37	0.12	0.10	0.16
Mean value (μ)	40.5	89747	32.9	0.36	0.12	0.11	0.16
Standard deviation (σ)	2.1	2538	2.2	0.04	0.04	0.04	0.01
Coef. of variation (%)	5.2	2.8	6.7	11.7	31.5	42.0	5.0

recorded after a significant reduction of the effective confinement (see $t \geq 50s$ in Figs. 4 and 5). A better description of such large permanent strains could have been achieved through the introduction of additional "damage" parameters, such as those proposed by Yang et al. [22]. As mentioned in the Introduction, such additional parameters were not considered as it is beyond the scope of this work since this study mainly focuses on the acceleration and excess pore pressure response, and the inclusion of additional parameters would increase the complexity in the analysis. The computed and experimental effective stress paths show a good agreement between them (Fig. 6). The contractive tendency is

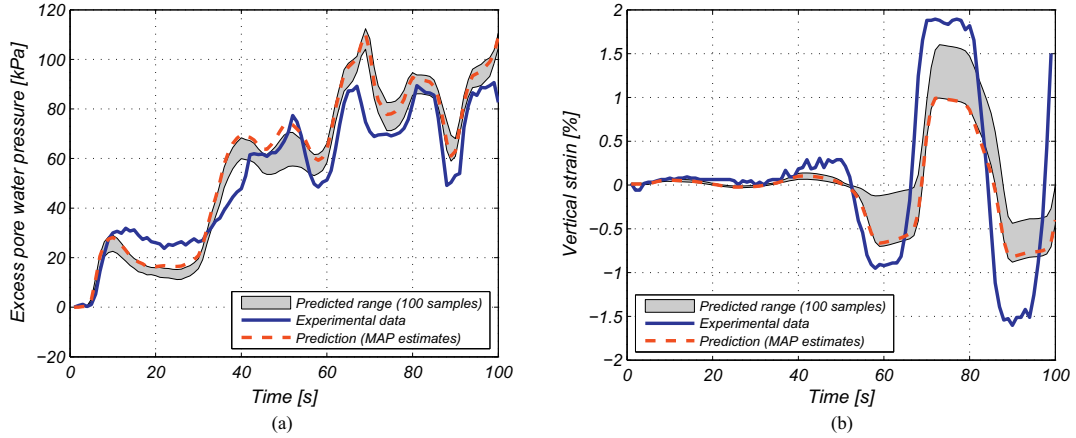

Fig. 4. (a) Excess pore water pressure, and (b) vertical strain response for the experimental triaxial test and numerical simulations.

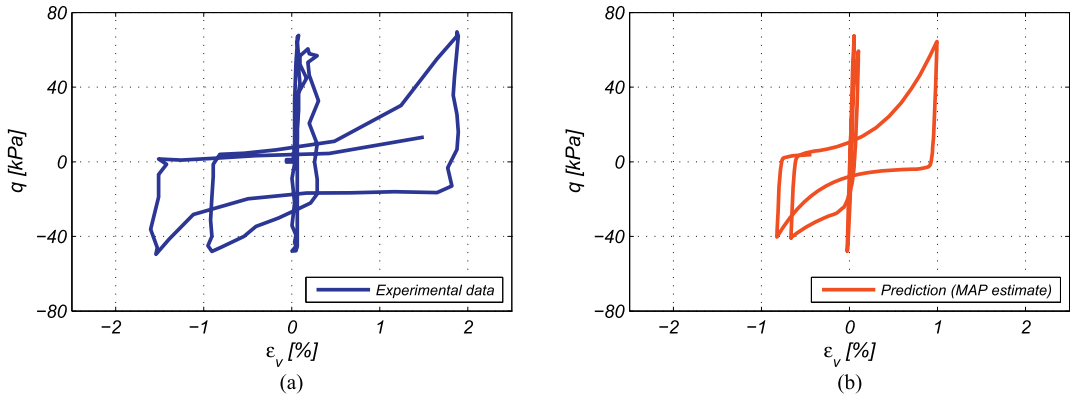

Fig. 5. Stress-strain cycles for (a) the experimental triaxial test, and (b) numerical simulation using maximum values of the posterior distributions of parameters.

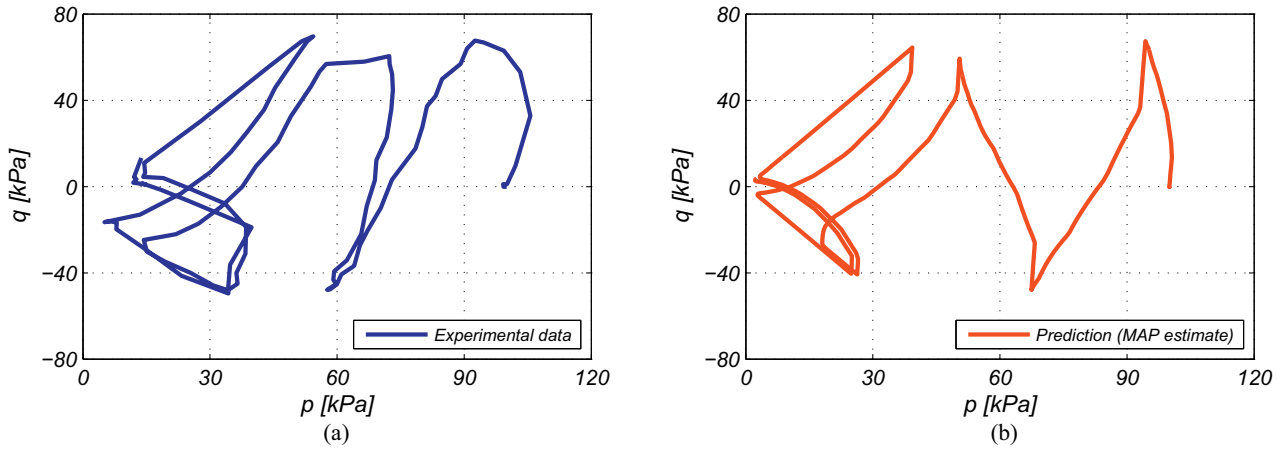

Fig. 6. Effective stress paths for (a) the experimental triaxial test, and (b) numerical simulation using maximum values of the posterior distributions of parameters.

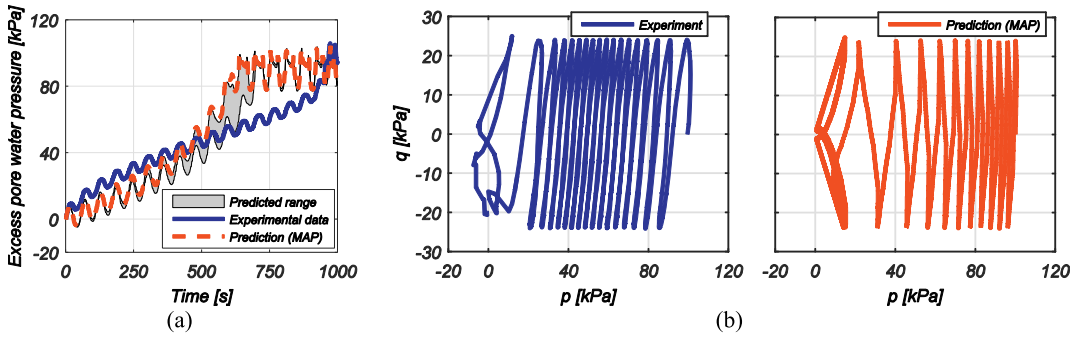

Fig. 7. (a) Excess pore water pressure, and (b) effective stress paths for the experimental triaxial test and numerical simulations.

well captured by the numerical model, leading to a reduction of effective confining stress with cyclic loading that closely matches the experimental results. The dilative phase of the numerical simulations is also in close agreement with the experiment, exhibiting a regain of effective confinement and an increase in deviatoric stress as the stress state surpasses the PT surface. Ranges of computed responses show relatively little scatter for the predicted excess pore pressure response for the selected samples of Θ_m (Fig. 4); computed vertical strain responses show a somewhat larger scatter mainly for predictions of large strains at low effective confinement.

The implementation of the Bayesian analysis has yielded an estimation of the model parameters describing the observed material behavior. The analysis has also quantified the estimation uncertainty for each of the model parameters. In this case, the associated uncertainty is stemming from one single triaxial test; if several tests had been used, the resulting uncertainty in the parameters estimation could have been higher due to the test-to test variability. The correlations between model parameters (observed in Fig. 3) evidenced a lack of uniqueness in the identification of an optimal set of model parameters, further increasing the uncertainty of the estimated parameters. The effects of including the uncertainty of the estimated parameters in the modeling of the dynamic response of the deposit are explored in the subsequent sections of this document.

4.3. Verification of updated model parameters using additional experimental tests

Results of the model updating were verified on two additional soil tests: a triaxial test and a direct simple shear test. Both tests were conducted using clean Ottawa sand similar to that described in Section

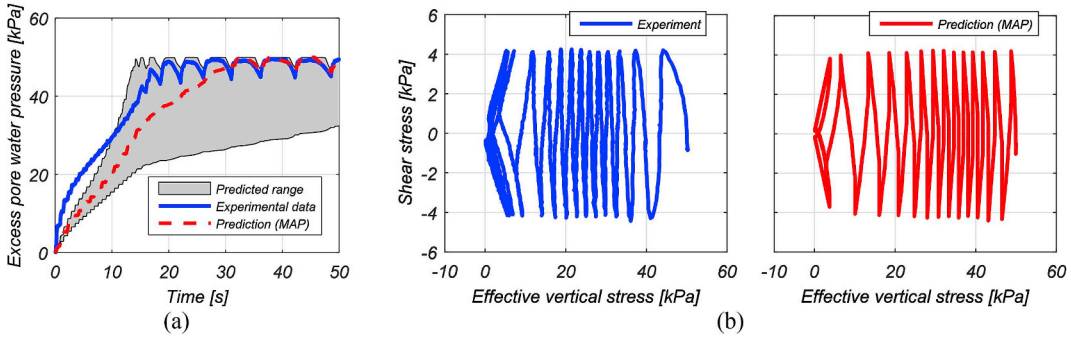

Fig. 8. (a) Excess pore water pressure, and (b) shear stress vs. effective vertical stress for the experimental direct simple shear test and numerical simulations.

2. The triaxial and direct simple shear tests had initial dry densities of 1560 kg/m^3 and 1576 kg/m^3, respectively. The relative differences between these achieved densities and the density of the triaxial test used for the calibration of the parameters is less than 2%. It should be pointed out that these tests have different values of initial confinement. The triaxial test was performed having an initial isotropic effective confinement of 100 kPa, while for the direct simple shear test an initial vertical effective pressure of 50 kPa was applied. More details on these experiments are given by Ochoa-Cornejo et al. [7,8], and Parra [68].

Fig. 7 and Fig. 8 show the excess pore water pressure responses and stress paths for both tests. The figures also show the numerical responses obtained by using MAP values of model parameters obtained from the calibration of the previous test, described in Section 4.2 (Table 2). Ranges for numerical responses computed for 100 randomly selected samples are also depicted in these figures. These randomly selected samples correspond to sets of parameters for which each of the model parameters were within one standard deviation of the mean values of the posterior distributions (Table 2). The computed stress paths (Figs. 7b and 8b) exhibit a behavior that is in agreement with recorded responses: both computed and experimental responses show an initial reduction of effective confining stresses with cyclic loading followed by a regain of effective confinement as the stress state surpasses the PT surface. Computed excess pore pressure responses also show a relatively good agreement with the experimental responses. For the triaxial test, the rates of pore pressure build up show some discrepancies; the implemented model yields a rapid increase in rate of pore pressure build up while the experimental response exhibits a fairly constant rate. The uncertainty of the calibrated model parameters led to ranges of computed responses for the triaxial test which showed little scatter, yielding a consistent modeled response. The range of modeled responses for the direct simple shear test, on the other hand, is significant. As observed in Fig. 8a, values of achieved excess pore pressure range between approximately 32 KPa and 50 kPa at the end of the loading ($t = 50$ s).

It is interesting to note that the variability of material parameters has different significance for different tests. The deviation stemming from the calibration of parameters using a triaxial test has resulted in a small level of uncertainty in the simulation of a different triaxial test, while yielding significant uncertainty in the simulated response of a direct simple shear test.

5. Verification and uncertainty propagation in the dynamic modeling of a soil deposit

In this section, the response of FE simulations of a soil deposit under dynamic base excitation is addressed to gain insight into the propagation of the uncertainty associated to the estimation of model parameters into this type of systems. The model consists on a 6 m saturated deposit of a uniform layer of the Ottawa sand described in Section 2. Two different cases are considered: (a) Case 1, in which the deposit is subjected to a base excitation consisting of 15 sinusoidal cycles with 2 Hz of frequency and peak acceleration of approximately 0.07 g, and (b) Case 2, which uses a base excitation consisting of 5 sinusoidal cycles with 2 Hz of frequency and peak acceleration of approximately 0.03 g. For each of the considered cases, FE simulations were performed for a collection of 100 sets of material parameters Θ_m selected from the samples generated for the estimation of the soil constitutive model parameters. These sets were randomly selected considering only sets of parameters for which each of the model parameters were within one standard deviation of the mean values of the posterior distributions. Numerical simulations results are compared with those obtained from reduced-scale centrifuge experiments.

5.1. Numerical model

The FE model was developed in OpenSees [53]. The deposit is modeled in 2D using a single column of six four-node elements of 1 m length with both displacement and excess pore pressure degrees of freedom. The base excitation is a horizontal acceleration at the base nodes. Displacement degrees of freedom at any given depth were tied together (both horizontally and vertically) to impose periodic boundaries, following modeling practices by Elgamal et al. [69] and McGann and Arduino [70]. Pore pressure was prescribed as zero at the surface, while the base and lateral boundaries were set as impervious [69]. Material behavior is simulated using the constitutive model described in Section 3. Given that the material model is pressure dependent, and that the density of the modeled sand is considered as constant throughout the deposit, the material behavior of the whole deposit is described by a single set of material parameters, $\Theta_m = [\phi \;\; G_{\max} \;\; \gamma \;\; \nu \;\; c_1 \;\; d_1]^T \in \mathbb{R}^{6\times 1}$. For each simulation, a set Θ_m is used, leading to an associated deposit response which is hereby assessed in terms of internal accelerations and excess pore pressure buildup. It should be mentioned that, unlike the simulated prototype deposits, an actual model (for instance a centrifuge model) is expected to exhibit small random variations of soil density in space, leading to a variation of the corresponding material parameters and a consequent uncertainty in the system response [45]. The effects of spatial variability as a source of uncertainty, however, are not being considered in this work, since it is focused on the evaluation of uncertainty stemming from the calibration of parameters of a selected material model. The assumption of a constant density throughout the deposit is therefore appropriate for the purposes of this work.

5.2. Description of the centrifuge tests

The corresponding reduced-scale tests were conducted in a laminar box under a 25 g gravity field using the geotechnical centrifuge facility at RPI. The models were constructed using Ottawa sand, which was dry pluviated and saturated following the standard procedures implemented at RPI [71,72]. The sand was deposited aiming to achieve a $D_r = 40\%$, matching the triaxial test described in Section 2; however, as mentioned above, a small degree of spatial variability in the soil density

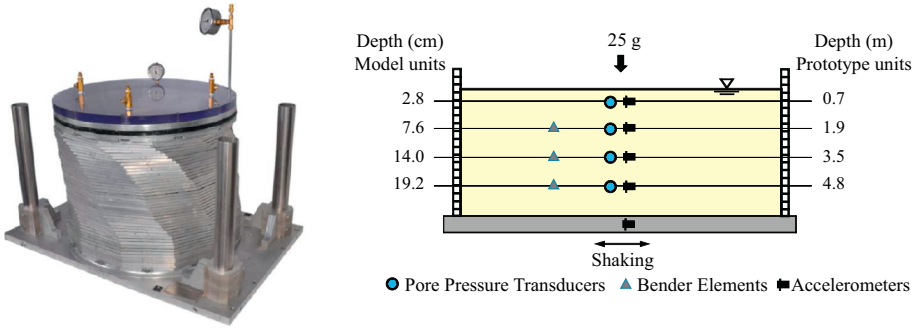

Fig. 9. Laminar container and configuration of the instrumentation used for the centrifuge test El-Sekelly [73].

is expected given the inherent limitations of physical modeling [45]. The height of the soil models was 24 cm, representing a soil deposit prototype with a depth of 6 m at 25 g. Hereafter, prototype units are employed when discussing centrifuge experiment results. The deposits were subjected to the two base excitations (Case 1 and Case 2). The response of the soil deposits was monitored using accelerometers, pore pressure transducers, and bender elements. It should be noted that the model was subjected to base acceleration in only one direction (1D). The acceleration in the direction perpendicular to the input motion was monitored and was found to be negligible. A photo of the laminar container and a sketch of the configuration of the sensors used in the experiment are shown in Fig. 9. More details about the experimental setup are given by El-Sekelly [73].

5.3. Verification analysis and uncertainty propagation

Fig. 10 displays the acceleration response recorded from the centrifuge tests along with a range of numerically simulated acceleration time histories using the selected sets of θ_m for cases 1 and 2. A generally good agreement is achieved between numerical predictions and recorded responses for both cases. The following observations can be made regarding the acceleration response:

- For Case 1, recorded accelerations are observed to decrease significantly near the surface ($z = 1.9$ m) after approximately $t = 5$ s, indicating the onset of liquefaction. Computed accelerations retain some residual strength which allows for small accelerations despite having reached values of pore pressure indicating liquefaction, as presented Fig. 11. At mid-depth ($z = 3.49$ m), recorded accelerations depict sudden spikes. Although these types of spikes are usually attributed to a dilative behavior of the soil [74,75], the absence of sudden drops in pore pressure suggests that the presence of spikes might be related to boundary effects, rather than to a dilative tendency in the soil. Computed acceleration time histories do not exhibit the presence of spikes, indicating that the stress state remained below the PT surface in the numerical simulations. In general, computed acceleration time histories are confined within a relatively narrow range at greater depths, but show a greater scatter at shallower depths. The scatter in computed accelerations seems to be mostly associated to the rate of decrease in acceleration amplitude.
- For Case 2, the amplitude of the achieved accelerations remains fairly constant throughout the deposit during the whole time history. It is observed that recorded accelerations are somewhat higher than the computed ones towards the top of the deposit. Very little scatter is observed in the computed accelerations. The scatter of computed acceleration time histories seems to be slightly larger towards the top of the deposit.

Computed and recorded pore pressure ratios, r_u, are shown in Fig. 11. Excess pore pressure ratio is defined as the ratio between the excess pore water pressure and the initial vertical effective overburden stress; a value of $r_u = 1.0$ indicates full liquefaction. The following observations can be made regarding the pore pressure response:

- For Case 1, recorded pore pressures show a rapid increase, reaching values of r_u close to 1.0 after approximately at 1 s of shaking at the upper depths of the soil deposit. At greater depths ($z = 4.6$ m), values of r_u are somewhat lower than those at shallower depths. Computed pore pressure ratios reach values of 1.0 throughout most of the depth of the deposit (approximately 2.0–5.0 m depth) after $t = 8$ s (see Fig. 12). The rates of pore pressure build up, however, varies significantly for the different numerical simulations. Fig. 12a shows a wide range of computed r_u values, particularly at $t = 5$ s, throughout the deposit.
- For Case 2, recorded and computed pore pressures increase gradually starting at the initiation of shaking, reaching maximum values at the end shaking (at approximately $t = 5$ s). In general, for both recorded and computed pore pressure responses, values of r_u are somewhat larger at shallower depths. Maximum values of r_u are well below 1.0 at all depths. This is not surprising given the relatively small amplitude of base acceleration. Computed pore pressure ratios exhibit significant scatter, which increases with the duration of shaking. Computed r_u values vary within ranges of around 0.1 to 0.25 throughout the deposit.

The observed variability in the simulated acceleration response seems relatively small, resulting in small discrepancies in the achieved peaks of accelerations at shallower depths, mainly during the time frame associated to the pore pressure buildup. The variability in the rates of pore pressure build up, however, was found to be significant for both tests. At $t = 5$ s, for instance, pore pressure ratios from the numerical simulations vary with a factor of about 2 at certain depths. It should be kept in mind that, as mentioned earlier, such variability stems from the calibration of a single triaxial test. If the parameter estimation would have been performed using multiple triaxial tests, the uncertainty in the estimated parameters would potentially have been higher due to the test-to test variability, probably leading to greater variability in the modeled response. It should also be noted that although the centrifuge experimental response provides a useful reference to assess the predictions of the numerical simulations, the numerical procedure aims at simulating the prototype behavior, not the physically modeled response. As other authors have mentioned [45], unavoidable difficulties during the experimental setup lead to a variability in the modeled acceleration and pore pressure response.

6. Conclusions

In this paper, experimental data collected from one undrained cyclic triaxial test performed on Ottawa sand were used to estimate the probability density functions of the parameters defining a pressure-dependent multi-yield constitutive model (PDMY02) employing a

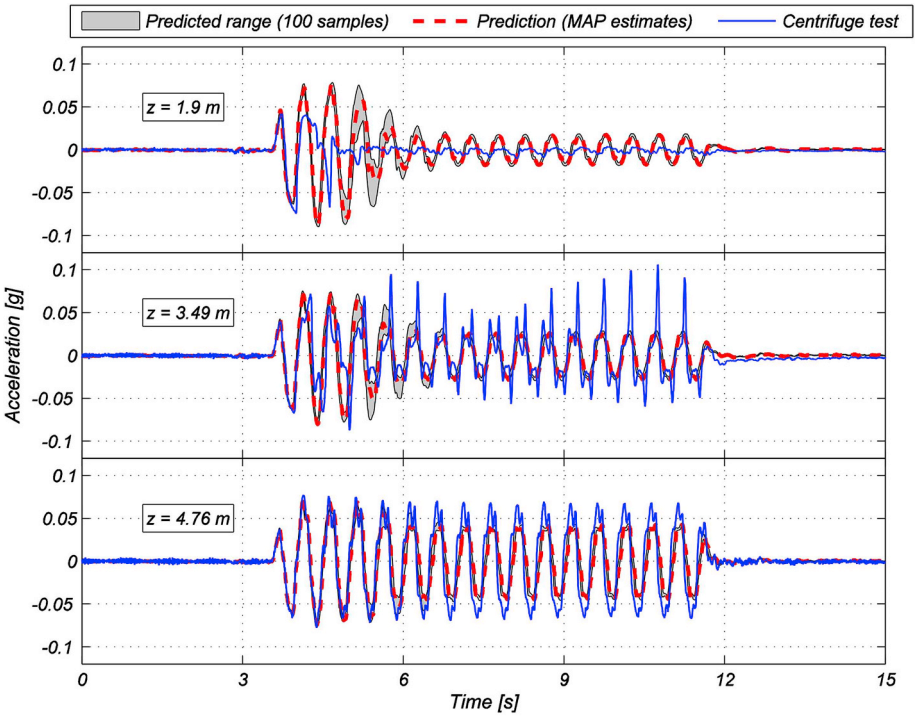

(a) Case 1

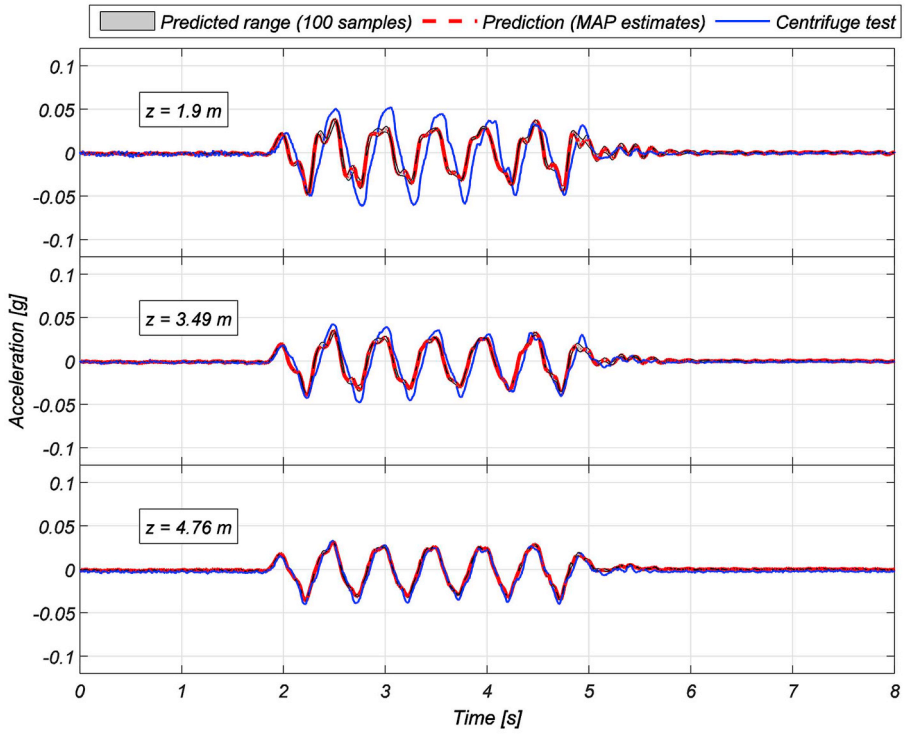

(b) Case 2

Fig. 10. Acceleration time histories for the experimental centrifuge test and numerical simulations. Depth $z = 0$ m corresponds to the surface of the experimental deposit (z is measured in prototype units).

Bayesian approach. Six model parameters, including the friction angle (ϕ), shear modulus at small strain ($G_{\max}$), phase transformation angle (ϕ_{PT}), Poisson ratio (ν), and material constants related to contractive and dilative behavior of the soil (c_1 and d_1, respectively), and one parameter related to the prediction error (σ_e) were estimated using normalized vertical strain (ε_v) and pore water pressure (u) as measured quantities. Posterior distributions of the model parameters allowed obtaining the marginal distribution of each estimated parameter and point (mean and maximum a posterior) and uncertainty (standard deviation and coefficient of variation) estimates. Correlation between different model parameters was observed, and the relationships (positive and negative correlations) were explained by the physical meaning

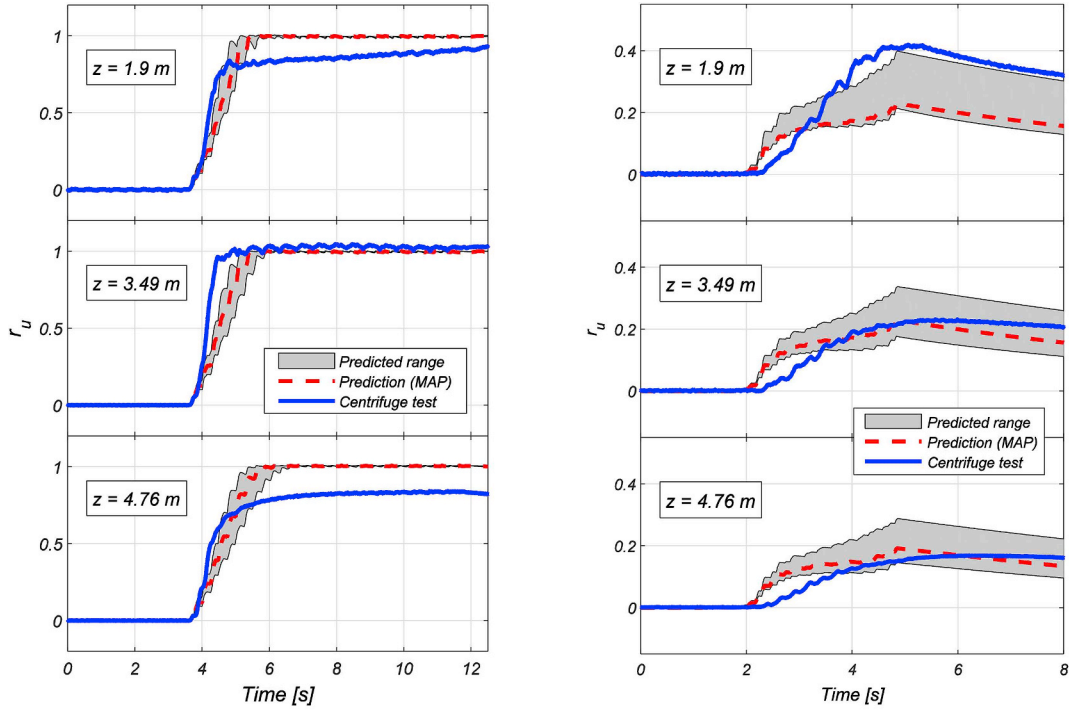

(a) Case 1 (b) Case 2

Fig. 11. Pore pressure ratio time histories for the experimental centrifuge test and numerical simulations. Depth $z = 0$ m corresponds to the surface of the experimental deposit (z is measured in prototype units).

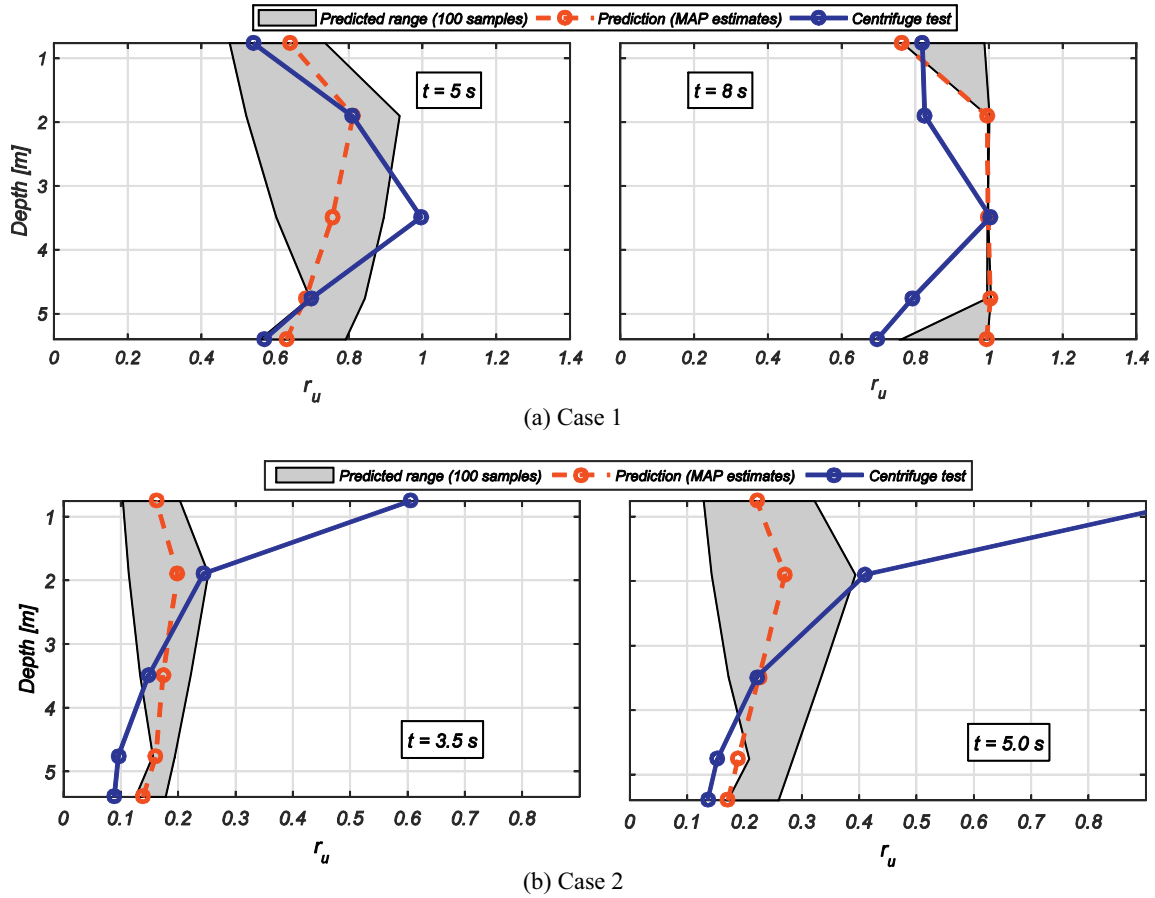

(a) Case 1

(b) Case 2

Fig. 12. Profiles of pore pressure ratio along depth for the experimental centrifuge test and numerical simulations at $t = 5.0\,s$, and $t = 8.0\,s$ (for Case 1), and at $t = 3.5\,s$, and $t = 5.0\,s$ (for Case 2).

of the constitutive model employed. Posterior distributions obtained from the Bayesian approach were used to explore the effects of the uncertainty in the estimated parameters on the predictive capabilities of a finite element (FE) model in simulating the dynamic response of a centrifuge soil model representing a 6 m depth saturated sand deposit. To this end, samples from the posterior distributions of the constitutive model parameters estimated using the cyclic triaxial tests were drawn, and the propagation of uncertainty in the numerically simulated acceleration and pore pressure responses was assessed and compared to the response of the centrifuge experiment. In general, a good agreement was observed between numerical simulations and the experimental response. Variability in the simulated acceleration response associated to the uncertainty in the model parameters estimation was relatively small, while variability in the rates of pore pressure build up was somewhat significant. It should be noted that the same Bayesian approach could be carried out in the evaluation of uncertainties using different material models.

The assessment of the credibility and capabilities of current computational tools is an unresolved challenge within the geotechnical community; in this context, this work offers a tool for the objective assessment of the capabilities and limitations that a certain material model has, given a set of data for calibration. The presented Bayesian inference framework allows for the proper quantification of uncertainty stemming from the calibration of the parameters of a given material model using laboratory data. Furthermore, it is shown that based on this quantified uncertainty, it is possible to quantify the uncertainty of the modeled dynamic response of a soil deposit resulting from the use of the Bayesian calibration procedure. Within the broader purpose of assessing predictive capabilities in liquefaction related problems, this work should complement ongoing and future efforts aimed towards the quantification of other sources of uncertainty such as the spatial variability of material properties or the repeatability of physical experimentation. A deeper understanding of the expected levels of uncertainty associated to different possible sources will result in more confidence in the available numerical tools and in a better judgement of modeled predictions of soil deposit responses.

Acknowledgements

This study was partially funded by the Department of Civil Engineering of the Universidad de Chile, making possible the leave of professor V. Mercado to the Universidad de Chile. R. Astroza acknowledges the financial support from the Chilean National Commission for Scientific and Technological Research (CONICYT), through FONDECYT-Iniciación research grant No. 11160009. F. Ochoa-Cornejo acknowledges the financial support of CONICYT, Project FONDECYT-Iniciación No. 11181252, and from Universidad de Chile, Project U-Inicia Code N° UI 24/2018.

References

[1] Mogami T, Kubo K. The behaviour of soil during vibration. Proc. 3rd international conference on soils mechanics and foundation engineering, zurich, Switzerland. 1953.
[2] Terzaghi K, Peck RB, Mesri G. Soil mechanics in engineering practice. John Wiley & Sons; 1996.
[3] Ishihara K. Liquefaction and flow failure during earthquakes. Geotechnique 1993;43(3):351–415.
[4] Verdugo R, González J. Liquefaction-induced ground damages during the 2010 Chile earthquake. Soil Dynam Earthq Eng 2015;79:280–95.
[5] Green R, Cubrinovski M, Cox B, Wood C, Wotherspoon L, Bradley B, Maurer B. Select liquefaction case histories from the 2010–2011 canterbury earthquake sequence. Earthq Spectra 2014;30(1):131–53.
[6] Cox B, Boulanger R, Tokimatsu K, Wood C, Abe A, Ashford S, Donahue J, Ishihara K, Kayen R, Katsumata K, Kishida T, Kokusho T, Mason H, Moss R, Stewart J, Tohyama K, Zekkos D. Liquefaction at strong motion stations in Urayasu City during the 2011 Tohoku-oki earthquake. Earthq Spectra 2013;29(S1):S55–80.
[7] Ochoa-Cornejo F. Cyclic behavior of sands with superplastic fines PhD. dissertation Purdue Uniersity; 2015.
[8] Ochoa-Cornejo F, Bobet A, Johnston CT, Santagata M, Sinfield JV. Cyclic behavior and pore pressure generation in sands with laponite, a super-plastic nanoparticle. Soil Dynam Earthq Eng 2016;88:265–79.
[9] Kramer S. Geotechnical earthquake engineering. Upper Saddle River, N.J.: Prentice Hall; 1996.
[10] Andrus RD, Stokoe II KH. Liquefaction resistance of soils from shear-wave velocity. J Geotech Geoenviron Eng 2000;126(11):1015–25.
[11] Youd T, Idriss I. Liquefaction resistance of soils: summary report from the 1996 NCEER and 1998 NCEER/NSF workshops on evaluation of liquefaction resistance of soils. J Geotech Geoenviron Eng 2001;127(4):297–313.
[12] Boulanger RW, Idriss IM. CPT and SPT based liquefaction triggering procedures. Davis, California: Department of Civil and Environmental Engineering, University of California; 2014.
[13] E. a. M. National Academies of Sciences. State of the art and practice in the assessment of earthquake-induced soil liquefaction and its consequences. Washington, DC: The National Academies Press; 2016.
[14] Wienbroer H, Rebstock D, Huber G. Shake-box tests. Int. Symp. On strong vrancea earthquakes and risk mitigation. 2007.
[15] Dobry R, Thevanayagam S, Medina C, Bethapudi R, Elgamal A, Bennett V, Abdoun T, Zeghal M, El Shamy U, Mercado V. Mechanics of lateral spreading observed in a full-scale shake test. J Geotech Geoenviron Eng 2010;137(2):115–29.
[16] Ecemis N. Simulation of seismic liquefaction: 1-g model testing system and shaking table tests. European Journal of Environmental and Civil Engineering 2013;17(10):899–919.
[17] Kutter B, Carey T, Hashimoto T, Zeghal M, Abdoun T, Kokkali P, Madabhushi G, Haigh S, d'Arezzo F, Madabhushi S, Hung W. LEAP-GWU-2015 experiment specifications, results, and comparisons. Soil Dynam Earthq Eng 2017;113:618–28.
[18] El-Sekelly W, Dobry R, Abdoun T, Steidl J. Centrifuge modeling of the effect of preshaking on the liquefaction resistance of silty sand deposits. J Geotech Geoenviron Eng 2016;142(6). 04016012.
[19] Kutter B. Dynamic centrifuge modeling of geotechnical structures. Tansportation research record 1992;1336:24–30.
[20] Kokkali P, Abdoun T, Zeghal M. Physical modeling of soil liquefaction: overview of LEAP production test 1 at Rensselaer Polytechnic Institute. Soil Dynam Earthq Eng 2017;113:629–49.
[21] Dobry R, Abdoun T, Thevanayagam S, El-Ganainy H, Mercado V. Case histories of liquefaction in loose sand fills during the 1989 Loma Prieta earthquake: comparison with large scale and centrifuge shaking tests. Seventh international conference on case histories in geotechnical engineering, chicago, IL. 2013.
[22] Yang Z, Elgamal A, Parra E. Computational model for cyclic mobility and associated shear deformation. J Geotech Geoenviron Eng 2003;129(12):1119–27.
[23] Taiebat M, Dafalias YF. SANISAND: simple anisotropic sand plasticity model. Int J Numer Anal Methods Geomech 2008;32(8):915–48.
[24] Boulanger R, Ziotopoulou K. PM4Sand (Version 3): a sand plasticity model for earthquake engineering applications. Davis, California: Department of Civil and Environmental Engineering, University of California; 2015.
[25] Fuentes W, Triantafyllidis T. ISA model: a constitutive model for soils with yield surface in the intergranular strain space. Int J Numer Anal Methods Geomech 2015;39(11):1235–54.
[26] Arulanandan K, Scott RF. Verification of numerical procedures for the analysis of soil liquefaction problems vols. 1 and 2. Taylor & Francis; 1993.
[27] Manzari M, Kutter B, Zeghal M, Iai S, Tobita T, Madabhushi S, Haigh S, Mejia L, Gutierrez D, Armstrong R, Sharp M, Chen Y, Zhou Y. LEAP projects: concept and challenges. Proceedings of the 4th international conference on geotechnical engineering for disaster mitigation and rehabilitation. 2015.
[28] Prevost J, Popescu R. An assessment of VELACS "Class A" predictions. Buffalo, NY, USA: US National Center for Earthquake Engineering Research (NCEER); 1994.
[29] Zeghal M, Manzari MT, Kutter BL, Abdoun T. LEAP: selected data for class C calibrations and class A validations. Safety and reliability: methodology and applications, vol. 117. 2014.
[30] Zeghal M, Goswami N, Kutter B, Manzari M, Abdoun T, Arduino P, Armstrong R, Beaty M, Chen Y, Ghofrani A, Haigh S. Stress-strain response of the LEAP-2015 centrifuge tests and numerical predictions. Soil Dynam Earthq Eng 2017;113:804–18.
[31] Assimaki D, Li W, Kalos A. A wavelet-based seismogram inversion algorithm for the in situ characterization of nonlinear soil behavior. Pure Appl Geophys 2011;168(10):1669–91.
[32] Zhang J, Tang WH, Zhang LM, Huang HW. Characterising geotechnical model uncertainty by hybrid Markov chain Monte Carlo simulation. Comput Geotech 2012;43:26–36.
[33] Groholski DR, Hashash YM, Matasovic N. Learning of pore pressure response and dynamic soil behavior from downhole array measurements. Soil Dynam Earthq Eng 2014;61:40–56.
[34] Ching J, Wang JS. Application of the transitional Markov chain Monte Carlo algorithm to probabilistic site characterization. Eng Geol 2016;203:151–67.
[35] Mercado V, El-Sekelly W, Zeghal M, Abdoun T, Dobry R, Thevanayagam S. Characterization of the contractive and pore pressure behavior of saturated sand deposits under seismic loading. Comput Geotech 2017;82:223–36.
[36] Akeju OV, Senetakis K, Wang Y. Bayesian parameter identification and model selection for normalized modulus reduction curves of soils. J Earthq Eng 2019;23(2):305–33.
[37] Astroza R, Pastén C, Ochoa-Cornejo F. Site response analysis using one-dimensional equivalent-linear method and Bayesian filtering. Comput Geotech 2017;89:43–54.
[38] Gras JP, Sivasithamparam N, Karstunen M, Dijkstra J. Strategy for consistent model parameter calibration for soft soils using multi-objective optimisation. Comput Geotech 2017;90:164–75.
[39] Dobry R, El-Sekelly W, Abdoun T. Calibration of non-linear effective stress code for

seismic analysis of excess pore pressures and liquefaction in the free field. Soil Dynamics and Earthquake Engineering. Soil Dynam Earthq Eng 2018;107:374–89.
[40] Phoon KK, Kulhawy FH. Characterization of geotechnical variability. Can Geotech J 1999;36(4):612–24.
[41] Whitman RV. Organizing and evaluating uncertainty in geotechnical engineering. J Geotech Geoenviron Eng 2000;126(7):583–93.
[42] Levasseur S, Malécot Y, Boulon M, Flavigny E. Soil parameter identification using a genetic algorithm. Int J Numer Anal Methods Geomech 2008;32(2):189–213.
[43] Zhou WH, Tan F, Yuen KV. Model updating and uncertainty analysis for creep behavior of soft soil. Comput Geotech 2018;100:135–43.
[44] Griffiths DV, Fenton GA. Probabilistic slope stability analysis by finite elements. J Geotech Geoenviron Eng 2004;130(5):507–18.
[45] El Ghoraiby M, Manzari M, Hamdar S. Effects of small variability of soil density on the consequences of liquefaction. Geo-risk 2017: reliability-based design and Code developments. 2017.
[46] Popescu R, Prevost JH, Deodatis G. 3D effects in seismic liquefaction of stochastically variable soil deposits. Risk and variability in geotechnical engineering. 2004.
[47] Montgomery J, Boulanger RW. Effects of spatial variability on liquefaction-induced settlement and lateral spreading. J Geotech Geoenviron Eng 2017;143(1). 04016086.
[48] Yang Z, Lu J, Elgamal A. OpenSees soil models and solid-fluid fully coupled elements. User's Manual. San Diego: University of California; 2008. Department of Structural Engineering.
[49] Krumbein WC, Sloss LL. Stratigraphy and sedimentation. San Francisco, CA: W.H. Freeman and Co.; 1963.
[50] Presti DL, Pedroni S, Crippa V. Maximum dry density of cohesionless soils by pluviation and by ASTM D 4253-83: a comparative study. Geotech Test J 1992;15(2):180–9.
[51] Cresswell A, Barton ME, Brown R. Determining the maximum density of sands by pluviation. Geotech Test J 1999;22(4):324–8.
[52] Zienkiewicz OC, Chan AHC, Pastor M, Schrefler BA, Shiomi T. Computational geomechanics with special reference to earthquake engineering. John Wiley & Sons; 1999.
[53] McKenna F, Fenves G, Scott M. Open system for earthquake engineering simulation. Berkeley, CA: University of California; 2000.
[54] Elgamal A, Zeghal M, Parra E, Gunturi R, Tang H, Stepp J. Identification and modeling of earthquake ground response—I. Site amplification. Soil Dynam Earthq Eng 1996;15(8):499–522.
[55] Elgamal A, Yang Z, Parra E. Computational modeling of cyclic mobility and post-liquefaction site response. Soil Dynam Earthq Eng 2002;22(4):259–71.
[56] Mroz Z. On the description of anisotropic work hardening. J Mech Phys Solids 1967;15(3):163–75.
[57] Prevost JH. A simple plasticity theory for frictional cohesionless soils. Int J Soil Dyn Earthq Eng 1985;4(1):9–17.
[58] Parra E. Numerical modeling of liquefaction and lateral ground deformation including cyclic mobility and dilation response in soil systems PhD. dissertation Troy, NY, USA: Department of Civil Engineering, Rensselaer Polytechnic Institute; 1996.
[59] Kondner RL. Hyperbolic stress-strain response: cohesive soils. J Soil Mech Found Div 1963;89(1):115–44.
[60] Ishihara K. Soil behaviour in earthquake geotechnics. Oxford engineering science series; 1996.
[61] Jaynes E. Information theory and statistical mechanics. Phys Rev 1957;106(4):620–30.
[62] Angelikopoulos P, Papadimitriou C, Koumoutsakos P. Bayesian uncertainty quantification and propagation in molecular dynamics simulations: a high performance computing framework. J Chem Phys 2012;137:144103.
[63] Papadimitriou C. Bayesian uncertainty quantification and propagation (UQ + P): state-of-the-art tools for linear and nonlinear structural dynamics models. In: Chatzi E, Papadimitriou C, editors. Identification methods for structural health monitoring. Cham: Springer; 2016.
[64] Beck J, Katafygiotis L. Updating models and their uncertainties Part I: Bayesian statistical framework. ASCE Journal of Engineering Mechanics 1998;124:455–61.
[65] Candy J. Bayesian signal processing: classical, modern, and particle filtering methods. Hoboken, NJ, USA: John Wiley & Sons; 2008.
[66] Ochoa-Cornejo F, Bobet A, Johnston C, Santagata M, Sinfield JV. Dynamic properties of a sand-nanoclay composite. Geotechnique 2019:1–54. (In Press).
[67] Neal R. Slice sampling. Ann Stat 2003;31(3):705–67.
[68] Parra A. Ottawa F-65 sand characterization PhD. dissertation Davis: University of California; 2016.
[69] Elgamal A, Yang Z, Parra E. Computational modeling of cyclic mobility and post-liquefaction site response. Soil Dynam Earthq Eng 2002;22(4):259–71.
[70] McGann C, Arduino P. Effective stress site response analysis of a layered soil column. 2011 [Online]. Available:. http://opensees.berkeley.edu/wiki/index.php/Effective_Stress_Site_Response_Analysis_of_a_Layered_Soil_Column, Accessed date: 15 August 2018.
[71] Gonzalez MA. Centrifuge modeling of pile foundation response to liquefaction and lateral spreading: study of sand permeability and compressibility effects using scaled sand technique PhD. dissertation Troy, NY: Rensselaer Polytechnic Institute; 2008.
[72] Abdoun T, Gonzalez M, Thevanayagam S, Dobry R, Elgamal A, Zeghal M, Mercado V, El Shamy U. Centrifuge and large-scale modeling of seismic pore pressures in sands: cyclic strain interpretation. J Geotech Geoenviron Eng 2013;139(8):1215–34.
[73] El-Sekelly W. The effect of seismic preshaking history on the liquefaction resistance of granular soil deposits PhD. dissertation Troy, NY: Rensselaer Polytechnic Institute; 2014.
[74] Zeghal M, Elgamal A. Analysis of site liquefaction using earthquake records. Journal of geotechnical engineering 1994;120(6):996–1017.
[75] Iai S, Morita T, Kameoka T, Matsunaga Y, Abiko K. Response of a dense sand deposit during 1993 kushiro-0ki earthquake. Soils Found 1995;35(1):115–31.